

Adjustment of a wind-driven two-layer system with mid-basin topography

by Magdalena Andres^{1,2}, Jiayan Yang¹ and Young-Oh Kwon¹

ABSTRACT

A linear primitive equations model is used to simulate spin-up of a two-layer ocean bisected by a meridional ridge. The ocean is forced with steady zonal winds east of the ridge. When wind-driven barotropic planetary Rossby waves propagate across the ridge, barotropic and baroclinic anomalies are generated as the barotropic flow adjusts. These ridge-generated anomalies propagate westward from the ridge as planetary Rossby waves and their arrival along the basin's western boundary modulates the western boundary current (WBC) transport and vertical structure. Model results suggest that at short (< 1 year) and long (> 10 years) delay relative to a change in wind stress curl, net WBC transport, T_{WBC} , is that predicted by the Sverdrup balance for a flat ocean, T_{Sv} , but at intermediate delay this balance is disrupted by arrival of the additional barotropic ridge-generated anomalies. The magnitude of the anomalous transport, T'_{WBC} , depends on the meridional deflection of the flow at the ridge relative to the length-scale over which wind stress curl varies. The timescale, t_{BT} , associated with adjustment at the ridge is a function of latitude, density contrast between layers and ridge width.

1. Introduction

During spin-up of a two-layer flat ocean, wind forcing generates barotropic and baroclinic responses, which propagate westward as long planetary Rossby waves (Veronis and Stommel, 1956). Barotropic responses propagate rapidly and establish a barotropic western boundary current (WBC), while baroclinic responses propagate westward slowly, eventually leaving an arrested lower layer and intensified upper layer in their wake (Anderson and Gill, 1975; Gill, 1982). When baroclinic signals arrive at the western boundary, they do not change the net transport there, but simply redistribute transport so it is carried in the upper layer. Despite this change in the vertical structure of the WBC during spin-up of a flat ocean to an equilibrium state, the WBC transport continually balances the interior Sverdrup flow throughout spin-up. This meridional WBC transport at a given latitude, T_{Sv} , is a function of the wind stress curl at that latitude, y :

$$T_{Sv}(y) = \frac{1}{\beta\rho_o} \int_{x_W}^{x_E} \vec{k} \cdot \nabla \times \vec{\tau}(x, y) dx. \quad (1)$$

1. Department of Physical Oceanography, Woods Hole Oceanographic Institution, 266 Woods Hole Road, MS 21, Woods Hole, Massachusetts 02543, USA.

2. Corresponding author *e-mail*: mandres@whoi.edu

Here β is the meridional gradient of the Coriolis parameter, ρ_o is the ocean's reference density, and \vec{k} is the unit vertical vector. Wind stress, $\vec{\tau}(x, y)$, is applied over a zonal width, W_w , with an eastern limit x_E and a western limit x_W .

Observations provide evidence of the baroclinic component of the ocean's wind-forced response. Satellite-observed sea surface height anomalies (SSHa) have been hindcast successfully using a $1\frac{1}{2}$ -layer reduced-gravity model (Qiu, 2003). Sea level variability as measured by tide gauge data from Bermuda is also well explained by a model of wind-driven first baroclinic mode Rossby waves (Sturges and Hong, 1995). In addition to this evidence from sea surface measurements, slow westward progression of wind-driven baroclinic Rossby waves is observed in the sub-surface ocean with historical hydrography (Price and Magaard, 1986; Deser et al., 1999). This slow adjustment gives rise to a long delay between changes in the wind forcing over the ocean interior and responses in the basins' WBCs and their extensions. Such delay is observed, for example, in the Kuroshio Extension's strength and position relative to wind stress curl anomalies over the eastern North Pacific (Qiu and Chen, 2005).

There is also observational evidence of the barotropic component of the ocean's response to wind forcing with observed ocean variability coherent with non-local wind forcing (Brink, 1989). Recent analysis of altimetry and hydrography from the western North Pacific's marginal seas suggests the baroclinic response (evident in sea surface- and pycnocline-slopes across the Kuroshio that lag the remote wind forcing by several years), is preceded by a rapid barotropic response with barotropic Kuroshio transport variability which is about one-third of the mean (Andres et al., 2011). This implies that fractured mid-basin topography like the Izu Ridge does not effectively block barotropic Rossby waves from reaching a basin's WBC.

Despite observational evidence of baroclinic and barotropic responses to wind forcing, each consistent with the Anderson and Gill (1975) formulation for a flat-ocean, there are unresolved issues related to the role of topography in shaping the ocean's response to wind-forcing. First, observations from the South Pacific subtropical WBC, the East Australia Current, suggest the delay between wind forcing and WBC response is too short to result from baroclinic Rossby wave propagation from the wind-forced region to the western boundary (Hill et al., 2008). Those observations suggest a three-year lag when 10 years are expected. While this observed lag is too short to result from the wind-forced baroclinic response, it is also too long to be associated with a purely barotropic response. This implicates interesting dynamics beyond those captured by Anderson and Gill (1975). Second, some modeling studies suggest that topography effectively blocks barotropic signals (Tanaka and Ikeda, 2004) thereby preventing them from reaching the WBC. Such results indicate either the observations of a rapid barotropic response along the North Pacific's western boundary noted above (Andres et al., 2011) are misinterpreted, or the barotropic mode is misrepresented by some models. Finally, there are regions where the $1\frac{1}{2}$ -layer reduced-gravity model, which excludes the barotropic mode by design, has insufficient skill to hindcast SSHa (Qiu, 2003). This suggests that processes in addition to wind-forced baroclinic Rossby wave propagation

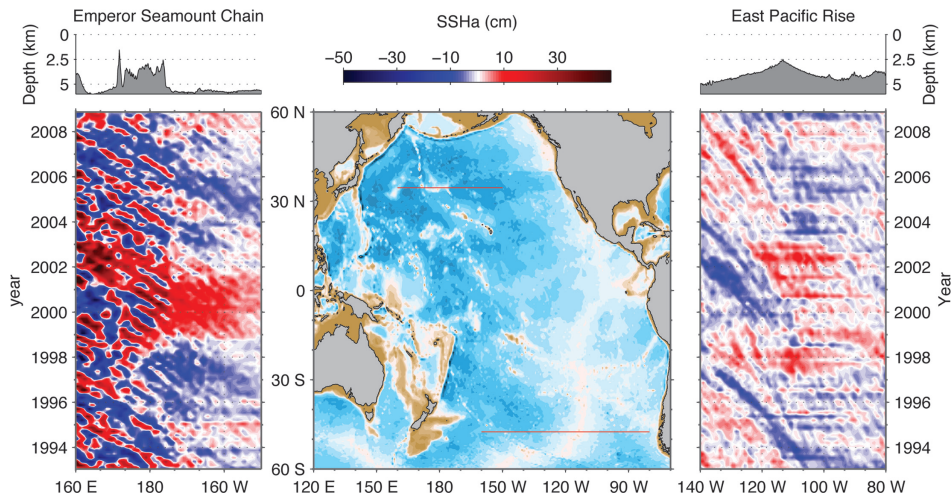


Figure 1. Center: Pacific bathymetry (Smith and Sandwell, 1994). Red lines indicate sections along which Hovmöller diagrams are shown. These cross the Emperor Seamount Chain at 34–35°N (left panel) and the East Pacific Rise at 47–48°S (right panel); shading indicates SSHa (cm). Depth sections showing the topography are above the respective Hovmöller diagrams.

contribute significantly to the SSHa signal. Propagation of barotropic Rossby waves and their interaction with topography may be such a process.

Satellite altimetry suggests that mid-ocean topography, like ridges and seamount chains, may modify the ocean's wind-driven response. Figure 1 shows Hovmöller diagrams of SSHa around the Emperor Seamount Chain and the East Pacific Rise, two major topographic features in the Pacific. In both cases, even though the sloped phase lines suggest that baroclinic activity is present throughout the region, it seems enhanced west of the topography. Genesis of baroclinic SSHa along ridges has also been noted by Chelton and Schlax (1996).

This altimetry and the unresolved issues noted above motivate the following questions, which are the focus of this paper. How does barotropic flow in a layered ocean contend with topography, especially mid-ocean ridges? What causes variability in WBC transport that appears related to wind-forcing, but with the “wrong” delay (i.e., too short to mark the arrival of wind-driven baroclinic Rossby waves but too long to be due to the arrival of wind-driven barotropic Rossby waves)? Does the interaction of barotropic flow with topography have a detectable expression in SSHa?

If the basin's western boundary is separated from the wind-forced region by a meridional ridge, first the wind-driven barotropic response and later the baroclinic response must contend with the ridge. Here we consider that part of the spin-up process during which a wind-driven barotropic signal interacts with the ridge and the flow in the two layers slowly adjusts due to the layers' coupled response to topography. (The eventual arrival of slowly propagating wind-driven baroclinic signals at a ridge and the subsequent adjustment have

been investigated for various cases—Barnier, 1988; Pedlosky and Spall, 1999; Tallieux and McWilliams, 2000; and Owen et al., 2002, 2005—and are not explored here.) We show that the adjustment to the wind-driven barotropic signal generates barotropic and baroclinic anomalies that propagate westward from the ridge (called ridge-generated anomalies here, to distinguish them from wind-forced responses generated directly under the wind patch). Arrival of barotropic ridge-generated anomalies at the western boundary disrupts WBC transport set by the Sverdrup balance and the baroclinic ridge-generated anomalies affect the WBC's vertical structure.

We use an idealized numerical model to explore 1) dynamics controlling this adjustment (locally at the ridge and remotely at the western boundary); 2) the timescale over which the adjustment occurs; and 3) the magnitude of the resulting disruption to the Sverdrup balance. The model is introduced in Section 2. Model results are presented in Section 3 and interpreted in context of baroclinic and barotropic ridge-generated anomalies. Section 4 discusses the underlying mechanisms and presents scales for the adjustment's duration and the associated WBC transport anomaly. Section 5 discusses implications of the model results for ocean observations.

2. Two-layer model

A linear primitive equations model is used to consider the spin-up of a two-layer ocean in response to a zonal wind stress. The model, detailed in Appendix A.1, has a free surface and both layers are active (the simplest form that can resolve the barotropic- and first baroclinic-modes in the presence of topography). In each layer, i , the model solves the depth-integrated linear shallow water equations on a beta-plane subject to mass conservation, where $i = 1$ for the upper layer and $i = 2$ for the lower layer.

Model variables are shown in Figure 2 and model parameters with their values are listed in Table 1. Wind forcing is applied away from topography where the unperturbed layer thicknesses are H_i and the bottom falls along $z = -H$. Bottom elevation over this reference level is η_b and is confined to the lower layer. The perturbed sea surface and interface elevations are η_1 and η_2 , respectively. Layer thicknesses, h_i , are $H_1 + \eta_1 - \eta_2$ in the upper layer and $H_2 - \eta_b + \eta_2$ in the lower layer. Initially (before wind forcing is applied), these are $h_1(0) = H_1$ and $h_2(0) = H_2 - \eta_b$. Layer thickness anomalies about this, h'_i , are $\eta_1 - \eta_2$ in the upper layer and η_2 in the lower layer. Total thickness, $h_1 + h_2$, is denoted as h .

The domain is a rectangular basin on a beta-plane centered on $\theta_0 = 30^\circ\text{N}$ ($y = 0$ km). The basin's meridional extent, Y , is 5,000 km. Results are first considered for an ocean whose zonal width, X , is similar to that of Pacific ($X = 10,000$ km). Then the analysis is continued with an ocean twice as wide ($X = 20,000$ km), to isolate those processes related to the impingement of the wind-driven barotropic flow on the ridge. This zonally-expanded basin geometry serves to delay the arrival of the wind-forced baroclinic signal at the ridge, as this shuts down lower-layer flow, thereby arresting the processes of interest in this study. The ocean reaches a maximum depth, $H = 4,000$ m with $H_1 = 800$ m and $H_2 = 3,200$ m. Reduced gravity, g' , is 0.01 m s^{-2} ($\Delta\rho = 1 \text{ kg m}^{-3}$).

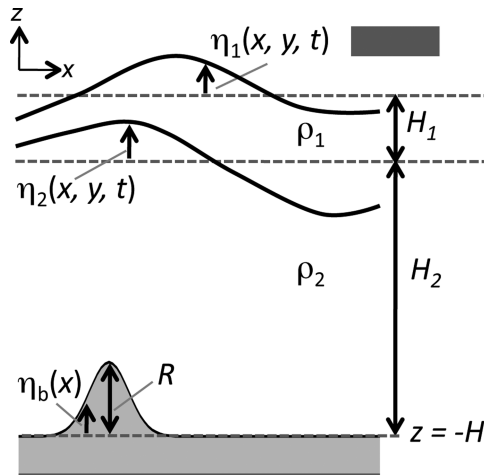


Figure 2. Model variables for a wind-forced two-layer ocean with a meridional ridge. Beneath the wind patch (grey rectangle) the unperturbed layer thicknesses are H_1 and H_2 and the total water thickness is H . Bottom elevation over a reference level ($z = -H$) is η_b and the ridge reaches to a crest height, R ($R = 0$ m for the flat-bottom model runs). Anomalies in sea surface and layer interface level are η_1 and η_2 . The schematic is not drawn to scale: η_1 is $O(1 \text{ cm})$ while η_2 is $O(10 \text{ m})$.

The bottom is configured either with a uniformly deep flat-bottom ($\eta_b = 0$), or with a Gaussian-shaped meridional ridge reaching to a crest of height, R , (Fig. 2) that spans the entire basin at $x = x_R$:

$$\eta_b = R \exp \left[\frac{-(x - x_R)^2}{2W_R^2} \right]. \tag{2}$$

The scale for the ridge’s zonal width, W_R , is 500 km.

The basin is forced with a time-invariant zonal wind stress on the upper layer, τ^x , initiated at $t = 0$. The stress has a Gaussian profile, and is centered on 30°N so wind stress curl is positive north and negative south of 30°N to generate a northern “subpolar gyre” and a southern “subtropical gyre”. The wind is applied east of the ridge in a band whose zonal width, W_w , is 2,000 km:

$$\tau^x(x, y) = 0.2 \text{ Nm}^{-2} \exp \left[\frac{-y^2}{2L_w^2} \right] \tag{3}$$

for $x_W \leq x \leq x_E$. In Equation 3, $y = -2,500$ to $2,500$ km and L_w , a meridional length scale for the wind, is 500 km. This forcing pattern, located well away from the boundaries, serves to minimize any waves excited along the boundaries that propagate very quickly around the basin as Kelvin waves.

Table 1. Model parameters.

| variable | definition | value(s) used |
|--------------|--|--|
| A | Horizontal viscosity coefficient | $2,000 \text{ m}^2 \text{ s}^{-1}$ |
| a | Earth's radius | 6,378 km |
| B | Biharmonic viscosity coefficient | $10^{12} \text{ m}^4 \text{ s}^{-1}$ |
| dt | Model timestep | 15 s |
| H | Ocean thickness | 4,000 or 4,800 m |
| H_1 | Thickness of unperturbed upper layer | 800 or 1,600 m |
| H_2 | Thickness of unperturbed lower layer (away from topography) | 3,200 m |
| L_w | Meridional length scale for the windstress | 500, 1,000, 1,500, or 2,000 km |
| R | Ridge height | 0, 300, 600 or 900 m |
| W_R | Scale for ridge's zonal width | 500 or 1,000 km |
| W_w | Zonal width over which wind stress is applied | 2,000 km |
| X | Zonal extent of ocean | 10,000 or 20,000 km |
| x_E | Eastern edge of wind patch | 8,000 or 19,000 km |
| x_R | Ridge location | 2,500, 3,600, 5,600 or 7,600 km |
| x_W | Western edge of wind patch | 6,000 or 17,000 km |
| Y | Meridional extent of ocean | 5,000 km |
| $\Delta\rho$ | Density contrast between layers | 1, 2 or 3 kg m^{-3} |
| Δx | Model resolution in x | 100 km |
| Δy | Model resolution in y | 100 km |
| θ_o | Model domain's central latitude | 30°N |
| ρ_o | Reference density | $1,028 \text{ kg m}^{-3}$ |
| τ^x | Maximum zonal windstress | 0.2 N m^{-2} |
| Ω | Earth's rotation rate | $7.2722 \times 10^{-5} \text{ s}^{-1}$ |

The model is used to investigate 1) propagation of barotropic and baroclinic anomalies (both those directly wind-forced and those generated at the ridge) and 2) the ocean's response to these anomalies in its WBC transport and vertical structure. Model output is used to track evolution of η_1 , η_2 , and WBC transport. The model is coarse resolution ($\Delta x = \Delta y = 100$ km), so WBC flow is tracked across a span of four grid points (400 km) to capture the model's whole boundary layer. With a higher model resolution and lower model viscosity, the WBC would be narrower, but the net transport would remain unaffected (Yang, 2003). Figure 3 shows the model domain and, as an example, η_1 and η_2 200 days after the wind is initiated. η_1 signals (red and blue contour lines) stretch west from the wind-forced region and are deflected southward over the ridge. η_2 signals (red and blue shading) are present both beneath the wind patch and where the η_1 contours intersect the ridge.

3. Model results

a. Differences between a flat ocean and an ocean with a ridge

First, to contrast how the ocean spins up with and without topography, model results from a flat ocean are compared with those from an ocean with a meridional ridge at $x_R = 2,500$

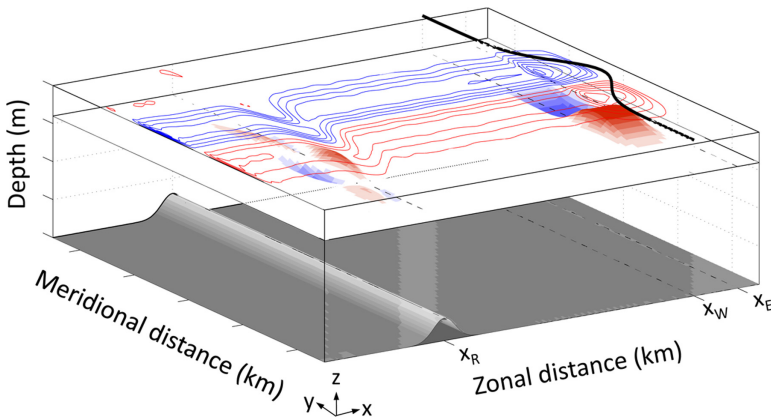


Figure 3. Model domain for a two-layer ocean with a meridional ridge. Dashed lines at x_W and x_E define region over which the wind stress is applied and the Gaussian zonal wind profile, τ_x , is denoted with the black curve. Colors show an example model-response 200 days after the wind is initiated: η_1 (contour-lines at 1 cm interval with red indicating elevated and blue indicating depressed surface) and η_2 (shaded surfaces with the vertical scale exaggerated by a factor of 10).

km. In both cases, $X = 10,000$ km and steady wind forcing, applied in the eastern basin from $x_W = 6,000$ km to $x_E = 8,000$ km, is initiated at $t = 0$.

i. Effects of a ridge on the WBC. The WBCs in both configurations exhibit a rapid wind-forced barotropic response followed years later by a wind-forced baroclinic response, but there are interesting differences in the configurations' WBCs that arise from the interaction of the (wind-forced) barotropic planetary Rossby waves with the meridional ridge. Figure 4 shows the 20-year transport time series at two 400 km sections spanning the WBCs for a flat-bottom ocean (panel a) and an ocean with a ridge of $R = 600$ m (panel b). These transport-sections lie 500 km north and south of the central latitude and fall along lines of maximum and minimum wind stress curl, respectively, in the "subpolar" and "subtropical" gyres. Since a WBC serves as return flow for interior transport, transport across the northern section is southward (negative transport, grey lines) while transport crossing the southern section flows northward (positive transport, black lines). Net (upper- plus lower-layer) WBC transports, T_{WBC} , from each configuration's southern section are shown in Figure 5.

With a flat bottom, the model-run is like the ocean considered by Anderson and Gill (1975). The model's barotropic response along the western boundary is fully developed rapidly, with velocities in the upper and lower layers that are equal and a ratio of layer-transport that is proportional to H_1/H_2 (Fig. 4a). When the wind-forced baroclinic Rossby waves arrive at the respective sections, the lower layer starts to shut down and transport becomes confined to the upper layer. The barotropic velocity structure persists until year-five in the southern section and year-nine in the northern section. This difference reflects

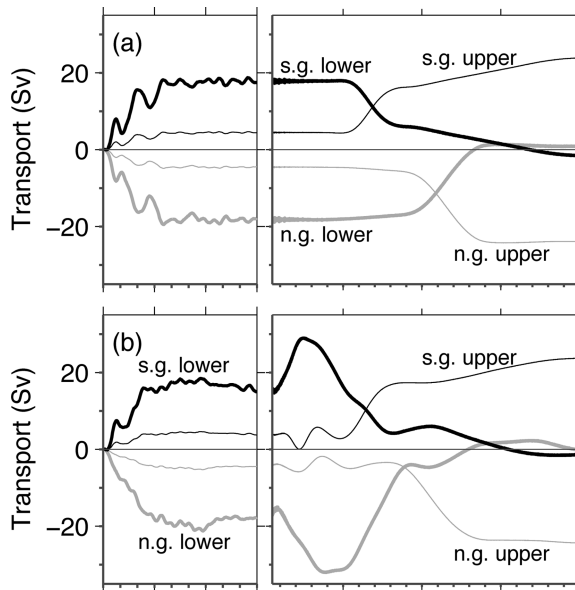


Figure 4. Time series of WBC transports for the northern gyre (grey lines) and southern gyre (black lines). Thin lines are upper layer transports and heavy lines are lower layer transports. Note, the x-axis time scale is stretched before day 180 to highlight the evolution of the barotropic response. Panels show results for (a) a flat-bottom ocean and (b) an ocean with a meridional ridge ($R = 600$ m).

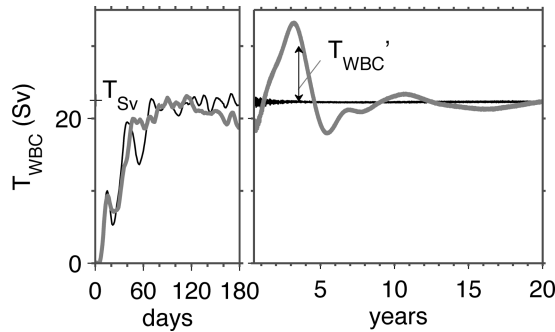


Figure 5. T_{WBC} at $y = -500$ km for a flat-bottom ocean (black curve) and an ocean with a meridional ridge of $R = 600$ m (grey curve). T'_{WBC} , indicated by the arrow, is $T_{WBC} - T_{SV}$.

the latitudinal dependence of baroclinic Rossby wave group speed, c . For long baroclinic Rossby waves, theory predicts:

$$c = -\beta (L_d)^2 \tag{4}$$

where L_d is the internal deformation radius. In the two-layer formulation:

$$L_d = \left(g' \frac{H_1 H_2}{H_1 + H_2} \right)^{1/2} / f. \quad (5)$$

At the model's southern section, where $L_d = 39$ km, the speed is about 3.3 km day^{-1} while at the northern section, where $L_d = 30$ km it is about 1.8 km day^{-1} . These model values are consistent with theoretical values predicted by Equation 4 (3.0 km day^{-1} and 1.8 km day^{-1} , respectively, with $\beta = 1.975 \times 10^{-11} \text{ m}^{-1} \text{ s}^{-1}$).

Since baroclinic Rossby waves carry no net transport, their arrival at the western boundary does not change T_{WBC} , just how this is distributed between upper- and lower- layers, consistent with Anderson and Gill (1975). This is demonstrated for the southern section with the black curve in Figure 5, which shows no change in T_{WBC} around year-five, despite arrival at the western boundary of the baroclinic signal.

For a flat ocean, a rapidly-established barotropic WBC is an expected result, however, the effect of topography on this mode is not obvious a priori and is considered next. As with the flat-bottom case, the barotropic response in an ocean with a ridge reaches the western boundary rapidly (Fig. 4b). Further, the lower layer throughout the domain is eventually shut down by baroclinic processes, thereby isolating the upper layer from the influence of topography. Hence T_{WBC} and the velocity-structure of the ocean's response within the first year and upon the final equilibrium state (achieved after year-10) are essentially identical between the cases (Figs. 4a and b).

Despite similarities with the flat-bottom model, the model with a ridge has two striking differences in its WBC, which occur between the initial response and the final equilibrium state. First, for a time, T_{WBC} is not T_{Sv} , predicted by Eq. 1 (Fig. 5). Anomalous transport, $T'_{WBC} = T_{WBC} - T_{Sv}$, is manifested at the southern section as a marked increase in T_{WBC} beginning in year-one and peaking around year-three. At the northern section a similar response (with opposite sign) peaks around year-four (compare Figs. 4a and b, heavy grey lines). Since the barotropic mode carries the transport, this result implies the arrival of an additional barotropic response at the western boundary. Second, the vertical structure of the WBC becomes bottom-intensified before lower-layer flow is eventually shut down by the arrival of baroclinic waves from the wind-forced region (Fig. 4, compare heavy lines in panel a to those in panel b).

These two differences are not confined to latitudes of maximum and minimum wind stress curl plotted in Figures 4 and 5, but are present along the whole western boundary. This is evident in space-time diagrams that compare evolution of the WBCs' lower-layer transport and T_{WBC} (upper plus lower layer) with and without topography (Fig. 6). In contrast to a flat ocean, where $T_{WBC} = T_{Sv}$ throughout spin up, T_{WBC} for the ocean with a ridge is not that predicted by the Sverdrup balance (Eq. 1) until the lower layer has been shut down by the wind-forced baroclinic Rossby waves and the system reaches final equilibrium. In the ocean with the ridge, this "equilibration time", t_{EQ} , for T_{WBC} to reach T_{Sv} (*i.e.*, when

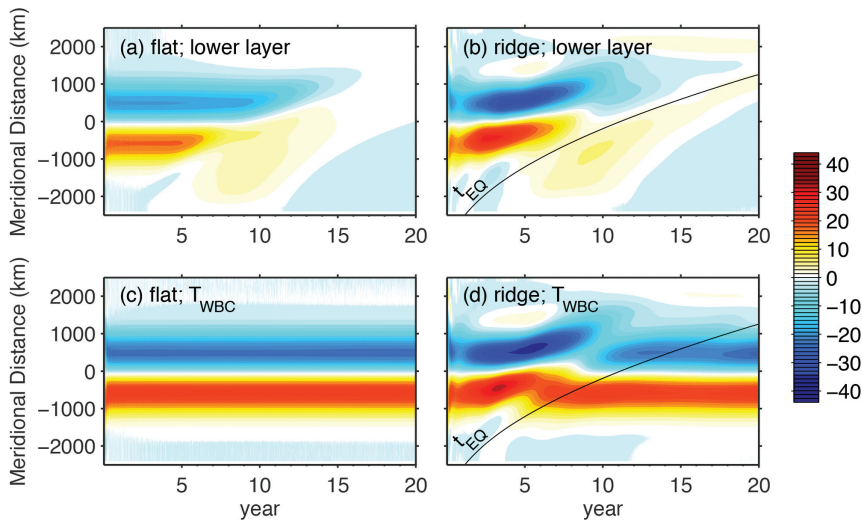


Figure 6. Space-time diagrams for WBC transport in a flat ocean (left panels) and an ocean with $R = 600$ m (right panels). Upper panels show transport carried in the lower layer. Lower panels show total transport (T_{WBC}). Black curves represent t_{EQ} for the ocean with a ridge (from Eq. 6).

$T'_{WBC} = 0$) depends on the baroclinic Rossby wave speed and can be expressed in terms of L_d (Eq. 5) and the distance from the western boundary to the wind patch, x_W :

$$t_{EQ} = \frac{x_W}{\beta L_d^2}. \tag{6}$$

As can be seen both from the model results contoured in Figure 6 and the theoretical prediction from Equation 6 (black curve), t_{EQ} increases poleward only if there is a ridge (panel d). In contrast, in the flat ocean, (T_{WBC}) reaches T_{Sv} well before lower-layer shut down (panel c) because the Sverdrup balance holds throughout spin-up and t_{EQ} is essentially zero (because – in contrast to an ocean with a ridge – for a flat ocean t_{EQ} depends on the very fast barotropic Rossby wave speed rather than on the slower baroclinic Rossby wave speed). While lower-layer shut-down is slower towards the north whether or not there is a ridge (panels a and b), latitude is only important for controlling t_{EQ} in the system with a ridge (via the dependence of L_d in Eq. 6 on f).

ii. *Effects of a ridge on η_1 and η_2 .* The WBC’s bottom-intensified vertical structure and anomalous transport (T'_{WBC}) result from westward propagating anomalies in sea surface height and interface depth that are generated where the wind-forced barotropic flow impinges on the ridge. At first, rapidly established η_1 signals stretch from the wind-forced patch to the western boundary (Figs. 7a and 8a). In the model with the ridge, these are deflected south across the ridge along f/h contours; in a flat ocean these are zonal. In both

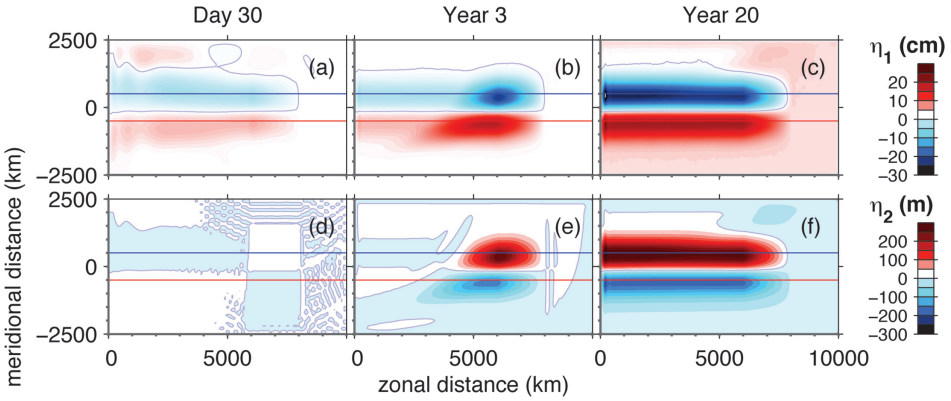


Figure 7. Snapshots of model output for flat-bottom ocean. Top row shows η_1 and bottom row shows η_2 with zero contour for each indicated with light blue curve. Red and blue lines highlight latitude of maximum and minimum wind stress curl, respectively (and latitudes for which WBC transports in Fig. 4 are plotted). $X = 10,000$ km, $R = 0$, $x_W = 6,000$ km and $x_E = 8,000$ km.

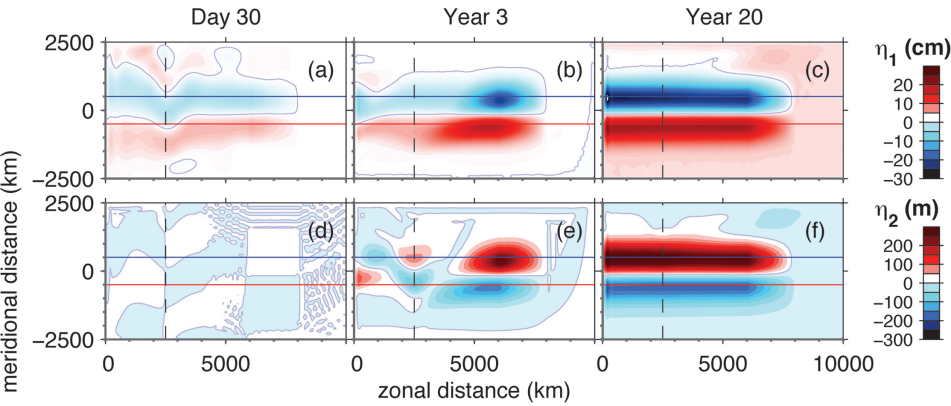


Figure 8. As in Figure 7, but for a model domain with a meridional ridge at $x_R = 2,500$ km indicated with dashed line. $X = 10,000$ km, $R = 600$ m, $x_W = 6,000$ km, and $x_E = 8,000$ km.

cases, these are eventually followed by larger amplitude wind-forced baroclinic η_1 signals (Figs. 7c and 8c), which propagate westward slowly together with η_2 signals of opposite sign (Figs. 7f and 8f). If there is a ridge however, this is preceded by the following: η_1 undulations at the ridge (generated where the initial barotropic flow followed f/h contours across the ridge) propagate towards the western boundary (Fig. 8b) in concert with η_2 anomalies (Fig. 8e) as baroclinic ridge-generated anomalies. In addition to these propagating baroclinic ridge-generated anomalies, a set of stationary η_2 anomalies is locked to the ridge, centered on the crest as a series of alternating high and low anomalies. These have no anomalous expression in the sea surface over the ridge. When the *wind-forced* baroclinic signals finally

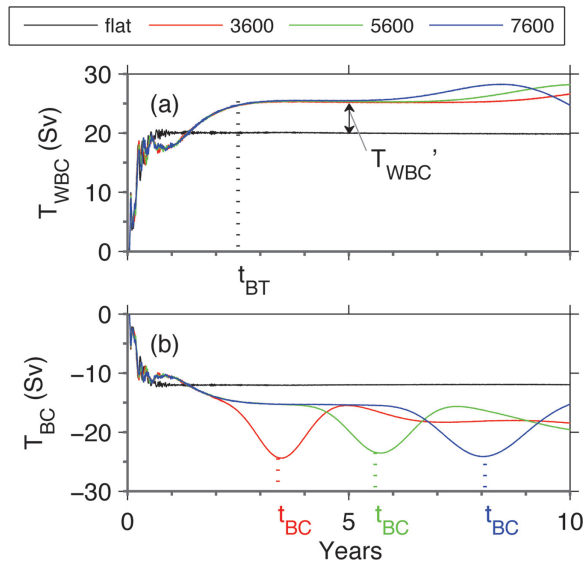


Figure 9. Response of WBC at $y = -500$ km to different ridge locations, x_R (indicated in legend in km), but the same forcing location ($x_W = 17,000$ km; $x_E = 19,000$ km). Panel (a) shows T_{WBC} . T'_{WBC} and t_{BT} , indicated on the plot, are both independent of x_R (see Section 4b for discussion of t_{BT}). Panel (b) shows the transport shear ($T_{BC} = H_1 u_1 - H_2 u_2$). For each x_R , t_{BC} is indicated on the plot. In these model runs $X = 20,000$ km.

do arrive at the ridge, lower-layer flow is shut down there and pressure associated with η_2 simply compensates that from η_1 so there is no pressure gradient in the lower layer (Fig. 8f).

b. Barotropic and baroclinic ridge-generated anomalies

The change in vertical structure shown in Figure 4 is caused by arrival of baroclinic ridge-generated anomalies at the western boundary while the increase in T_{WBC} shown in Figure 5 results from arrival of barotropic ridge-generated anomalies. (The subsequent decrease in T_{WBC} back to T_{Sv} is related to the *wind-driven* baroclinic waves' arrival at the ridge, but details of this process are not considered further here.) These barotropic and baroclinic ridge-generated anomalies are generated by interaction of barotropic (wind-forced) flow with topography. This is best demonstrated with a very wide basin ($X = 20,000$ km) in which the wind-forced region is far from the ridge (this delays the impingement of wind-forced baroclinic Rossby waves on the ridge). Figure 9 shows timeseries of T_{WBC} (“barotropic” or total, transport) and $H_1 u_1 - H_2 u_2$ (transport shear) at $y = -500$ km for various ridge locations (x_R) but the same forcing location. In all three cases: 1) the magnitude and timing of T_{WBC} is the same (T'_{WBC} reaches a steady level of 5 Sv around $t = 2.5$ yrs) and 2) transport shear is negative, indicating bottom-intensified flow (in contrast to positive transport shear, which occurs when wind-forced baroclinic Rossby waves arrest

the lower-layer and redistribute transport into the upper layer, beyond the time frame plotted in Fig. 9). Timing, t_{BC} , of the negative peak in transport shear, however, does vary with x_R and can be estimated by a form similar to Equation 6, but with x_W replaced with x_R :

$$t_{BC} = \frac{x_R}{\beta L_d^2} \quad (7)$$

According to this equation, the ridge-anomaly behaves as a long baroclinic Rossby wave propagating from the ridge to the western boundary. In Figure 9 $t_{BC} = 3.5, 5.7$ and 8.1 yr, respectively, as x_R increases from 3,600 to 5,600 to 7,600 km. The slope of x_R versus t_{BC} (not shown) gives an empirical speed of 2.4 km day^{-1} , in reasonable agreement with the theoretical long baroclinic Rossby wave speed at $y = -500 \text{ km}$ calculated from Equations 4 and 5 ($c = 3.0 \text{ km day}^{-1}$).

4. Discussion

The model results presented above suggest the following spin-up/adjustment process as the initial wind-forced barotropic (i.e., vertically-uniform) signal arrives at a ridge. During adjustment the layer-interface over the ridge deforms so the two layers no longer move as a barotropic column and, as a consequence, barotropic and baroclinic anomalies are generated at the ridge. The barotropic ridge-generated anomaly grows in amplitude throughout adjustment and propagates rapidly from the ridge crest to the western boundary where it causes anomalous transport (T'_{WBC}). In concert with this, the baroclinic ridge-generated anomaly develops and the interface displacement, together with the surface displacement, propagates westward as a baroclinic Rossby wave. When these baroclinic displacements arrive at the western boundary, they redistribute the WBC so transport is carried disproportionately by the lower layer, but their arrival does not change *net* WBC transport. Hence the anomalous transport remains steady until the eventual arrival of the wind-driven baroclinic Rossby waves causes a final adjustment and transport is finally that predicted by Equation 1 ($T_{WBC} = T_{SV}$).

This progression is illustrated with Hovmöller diagrams of η_1 and η_2 (Fig. 10). Along $y = -500 \text{ km}$ the fast initial wind-forced barotropic signal is evident only in η_1 (panel a) before $t = 0.25 \text{ yrs}$ (see the yellow shading stretching from the wind patch to the western boundary, highlighted with the solid black line). The shallow slope of the phase line indicates rapid propagation. This wind-driven barotropic flow impinges on the ridge at $x_R (= 5,600 \text{ km})$, where three additional signals are evident: 1) a stationary η_2 anomaly with vertical phase line (i.e., not propagating) centered on the ridge crest and with no corresponding anomalous η_1 expression; 2) a baroclinic anomaly with η_1 and η_2 signals that slowly propagate together towards the western boundary as indicated by the steeply sloped phase lines (these arrive at the western boundary around $t_{BC} = 6 \text{ yr}$, consistent with the green curve in Fig. 9b); and 3) a barotropic signal (evident by the shallow phase lines with orange shading in η_1 , but not discernable in η_2) radiating from the ridge with the amplitude of this

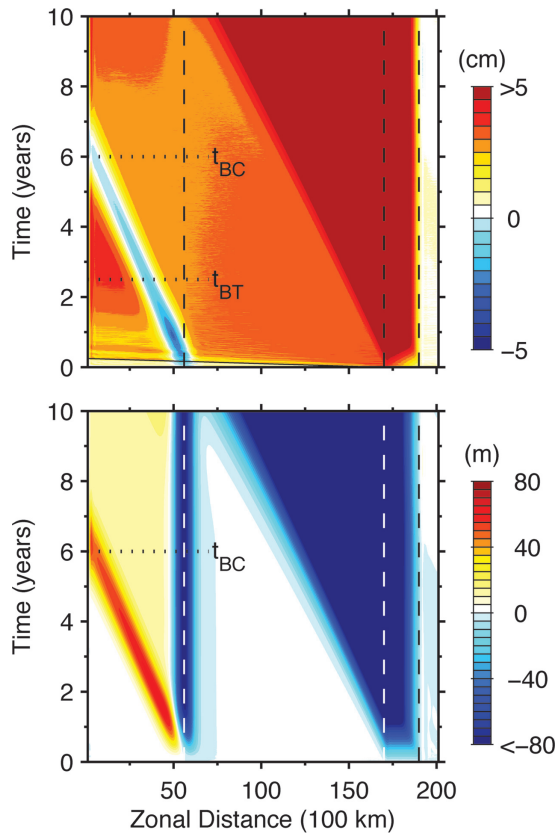


Figure 10. Hovmöller diagrams along $y = -500$ km showing η_1 in panel (a) and η_2 in panel (b). Dashed lines indicate ridge crest ($x_R = 5,600$ km) and edges of wind patch. t_{BT} and t_{BC} are indicated on the plots (see Sections 4b and 3b, respectively). Solid black line in (a) highlights propagation of the wind-driven barotropic signal from the wind patch to the western boundary before $t = 0.25$ yr. $X = 20,000$ km, $R = 600$ m, $x_R = 5,600$ km, $x_W = 17,000$ km, $x_E = 19,000$ km.

barotropic signal increasing until $t = 2.5$ yr. While this barotropic ridge-generated anomaly is subtle (its maximum amplitude is only a few centimeters), it is critical since it is the cause of the anomalous WBC transport that peaks at $t = 2.5$ yr (Fig. 9a).

To explain why the flow at the ridge must evolve as described above, we consider the dynamics in each layer and the coupling between the layers. Coupling occurs via vertical velocities w that displace the layer interface causing water column stretching and squashing. Once the interface no longer moves (i.e., when $\partial\eta_2/\partial t = 0$), flow in each layer is at equilibrium and the system is fully-adjusted at the ridge. In this sense, there are two different equilibria at the ridge during spin-up: 1) the first is reached after the adjustment to the rapid wind-driven barotropic signal and remains until the arrival of the slow wind-driven

baroclinic signal when $t \approx t_{EQ}$ (i.e., with t given by Eq. 6, but with the distance between the wind patch and the ridge, $x_W - x_R$, in the numerator) and 2) the second is reached after the adjustment to the slow wind-driven baroclinic signal. (The latter is the analog to Anderson and Gill, 1975 lower-layer shut-down for a flat ocean and is not considered further here.) For an ocean with a ridge, the upper-layer flow over the ridge is zonal in both equilibrium states. In contrast, the lower-layer flow is along f/h_2 contours in the first equilibrium but it is at rest in the final equilibrium. Below we consider the details of the first equilibrium state and then describe how the adjustment to this equilibrium occurs. Furthermore, we use scaling to determine what sets 1) the adjustment time scale t_{BT} (given in Eq. 11) and 2) the magnitude of the anomalous WBC transport T'_{WBC} (given in Eq. 19).

a. The barotropic flow's adjustment at the ridge

The adjusted flow at the ridge is geostrophic (and non-divergent with $\partial\eta_2/\partial t = 0$) and is dictated by potential vorticity conservation in each layer (friction is weak everywhere except along the western boundary). Thus, as mentioned above, flow in the upper layer is along f/h_1 contours while that in the lower layer is along f/h_2 contours (Fig. 11, lower right panel). The upper layer's path is independent of the ridge, oriented zonally as if flowing over a flat ocean (implicit in the linear model used here, is that interface displacements are small relative to the thickness of layer-1: $\eta_2 \ll H_1$ so $h_1 \approx H_1$). Where the lower layer thins over the ridge flank, fully-adjusted lower-layer flow is deflected southward and its speed must increase due to mass conservation. (Since the distance of southward deflection at the crest, Δy , is latitude-dependent, the flow's cross-sectional area is constricted not only by topography but also by horizontal compression of f/h_2 contours over the ridge; see Appendix A.2 for the derivation of Eq. A-6 describing this.) This increased flow must be supported by a pressure gradient. This cannot be provided by a tilted sea surface as this would cause increased flow in both layers, but is provided instead by a tilted layer interface. On the downstream side of the ridge crest where h_2 increases along the flank and the flow slows, this tilting is relaxed. This is consistent with the stationary η_2 anomalies, with no concomitant expression in η_1 , centered on the ridge crest as observed in the model results during the first equilibrium (Fig. 11, upper-right panel).

To reach this equilibrium, the flow must evolve from the initial barotropic (vertically uniform) state (Fig. 11, lower left panel). This initial flow along f/h contours is supported by pressure gradients that arise from the sea-surface height (η_1) gradients. Furthermore, this initial flow must be faster at the crest than in the flat regions (due to mass conservation) in both layers because the flow is vertically uniform. With topography only in the lower layer, this causes convergences and divergences in the upper layer over the ridge, thereby deforming the layer interface so $\partial\eta_2/\partial t \neq 0$ and coupling the layers through w (Fig. 11, upper-left panel). As the interface gets deformed and η_2 anomalies continually provide more of the pressure gradient required to support lower-layer flow, the upper-layer gradually decouples from topography (long before the arrival of the wind-forced baroclinic Rossby waves), flow in the upper-layer slows, and the sea surface tilts across the ridge relax somewhat. η_1

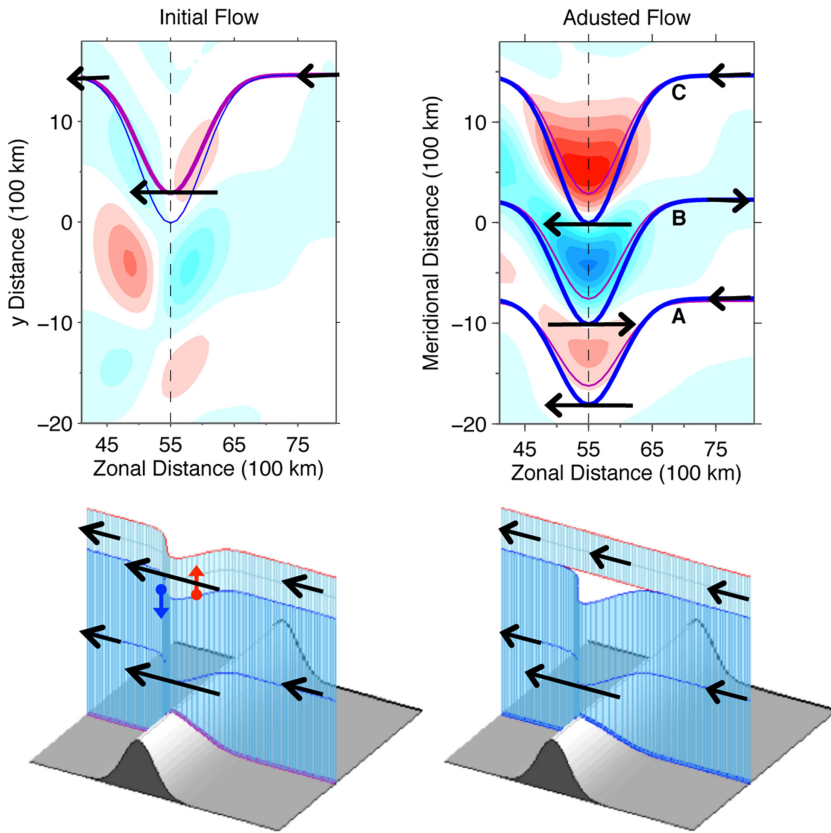


Figure 11. Flow evolution at a ridge from an initial state (left panels) to the fully-adjusted state (right panels). Upper panels show plan view of η_2 (heaved surfaces shaded red and depressed surfaces blue) straddling the meridional ridge crest (dashed line) on day-200 (left panel) and year-four (right panel); contours at 10 m interval. Constant f/h (purple) and f/h_2 (blue) are shown. Lower panels indicate schematically the flow in each layer. Initial flow: black arrows in the upper left panel indicate the vertically-uniform initial barotropic flow constrained to follow an f/h contour; bottom left panel shows the flow along an f/h contour with black arrows indicating upper- and lower-layer (vertically uniform) flows resulting from sloped η_1 . This flow is divergent/convergent in the upper layer and leads to vertical flow on the ridge flanks thereby deforming the layer interface (indicated with red and blue arrows). This decouples the layers, allowing the upper-layer η_1 -anomaly to propagate westward with the η_2 -anomaly from the ridge's western flank (see Fig. 12). Adjusted flow: in the right upper panel the arrows indicate the lower-layer flow, which speeds up over the crest. Right lower panel shows flow along contour A (or C) in both layers with lower layer flow deflected along f/h_2 contours and the upper layer flowing zonally across the ridge along f/h_1 . Model parameters as in Figure 10.

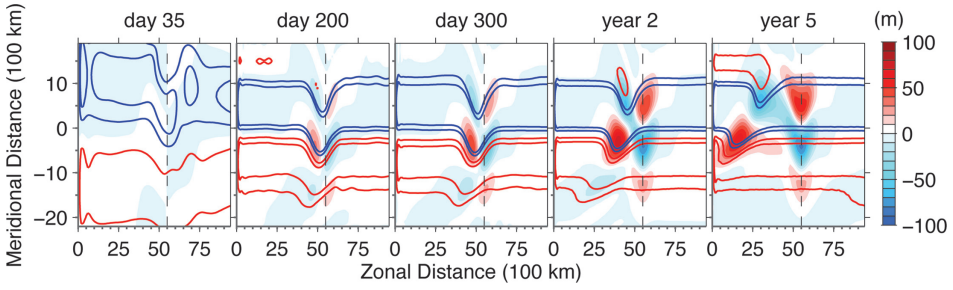


Figure 12. Snapshots showing evolution of stationary and propagating baroclinic ridge-anomalies. Shading indicates η_2 : blue is depressed interface, due to convergence in the upper layer; red is heaved interface due to divergence in the upper layer. Sea surface elevation is indicated by red and blue η_1 -contours at 1 cm and 2 cm (red) and -1 cm and -2 cm (blue). Dashed line indicates ridge crest. Model parameters as in Figure 10.

anomalies propagate westward, together with η_2 anomalies, as baroclinic ridge-generated anomalies (Fig. 12). Throughout this adjustment, the barotropic part of the total η_1 signal grows and radiates rapidly along f/h contours towards the western boundary leading to anomalous transport there (T'_{WBC}).

b. Adjustment time scale

From the description of the adjustment process in section 4a, it is clear that t_{BT} , the time scale for the initially-barotropic flow to fully adjust to the first equilibrium, is related to build up of interface displacements over the ridge. At $t = t_{BT}$, η_2 at the ridge crest reaches steady values (*i.e.*, $\partial\eta_2/\partial t = 0$). In addition, since the propagation of the barotropic signal from the ridge to the western boundary is very fast, T'_{WBC} on the western boundary has grown to its peak amplitude at $t \sim t_{BT}$ (Fig. 9a). These consequences of adjustment, both regulated by the same t_{BT} , each occur at a different latitude (y at the western boundary and y_S at the ridge crest) connected by a common f/h contour. In the following we develop the procedure for deriving a scale for t_{BT} (the final result is given in Eq. 11) and discuss the implication of this scale.

To develop scaling for t_{BT} , we consider the layer interface at the ridge. The adjustment time here depends on the magnitude and rate of interface displacement, $\Delta\eta_2$ and \bar{w} , as follows:

$$t_{BT} = \frac{\Delta\eta_2}{\bar{w}}. \tag{8}$$

Here \bar{w} is a measure of the interface’s average vertical velocity over the ridge flank during adjustment. The scale for \bar{w} is determined from mass conservation applied to the adjusting flow in layer-1:

$$\bar{w} = \frac{w(0) + w(t_{BT})}{2} \sim \frac{H_1(u_1(x_R, y_S, t = 0) - u_1(x_F, y, t = 0))}{W_R} \tag{9}$$

where $w(0)$ is the interface's initial vertical velocity and $w(t_{BT})$ is the interface's vertical velocity after adjustment, which is by definition zero. Upper-layer horizontal velocities at the ridge crest (x_R) and in the flat region between the wind patch and the ridge (x_F) associated with the initial flow are $u_1(x_R, y_S, t = 0)$ and $u_1(x_F, y, t = 0)$, respectively (Fig. 11, left panels). The velocity difference in the R.H.S. of Eq. 9 leads to the divergence or convergence in the upper layer over the ridge flank that drives the interface displacement. W_R is a length scale for the zonal width of the ridge flank (see Eq. 2); this is the distance over which this divergence or convergence occurs.

To determine $\Delta\eta_2$ in Equation 8, the thermal wind equation for a layered system (Margule's relation) is applied to the fully-adjusted flow at the ridge crest. This scales to give:

$$\frac{\partial\eta_2}{\partial y} = \frac{f}{g'}\partial u \sim \frac{\Delta\eta_2}{L_w} \sim \frac{f}{g'}(u_2(x_R, y_S, t_{BT}) - u_1(x_R, y_S, t_{BT})), \quad (10)$$

where $\partial y \sim L_w$. L_w is the meridional length scale over which the wind stress varies (see Eq. 3). The velocity difference on the R.H.S. of Equation 10 is the vertical shear of the adjusted flow at the ridge crest.

Plugging Equations 10 and 9 into Equation 8 gives a time scale for the adjustment to the first equilibrium:

$$t_{BT} \sim \frac{L_w W_R f}{2H_1 g'} u^*. \quad (11)$$

Here u^* is the ratio of the vertical shear of the *adjusted* zonal flow at the ridge crest to the *initial* horizontal divergence or convergence in layer-1 on the ridge's flank. (The full expression for u^* is given in Appendix A.3 as Eq. A-9) At a given latitude y , u^* is related to the zonal flow in the flat region between the wind patch and the ridge (x_F) at three different latitudes and thereby also to the wind stress curl at three different latitudes (Fig. 13): y_S (the latitude of zonal steady-state flow in layer-1), y_N (the latitude at which steady-state flow in layer-2 originates following f/h_2) and y (the latitude at which initial deflected flow in layer-1 originates following f/h). These connections between u_i at the ridge with u_i at x_F are developed in Appendix A.3 and described by Equation A-10.

We compare the scaling for t_{BT} in Equation 11 with output from the numerical model for a range of parameters (Fig. 14, Table 2). For a few tests, the ratio of modeled t_{BT} to that predicted from Equation 11 reaches 2.2 (*e.g.*, experiments 5 and 7 listed in Table 2) and the scaling in Equation 11 under predicts t_{BT} . For these cases, it is likely that the simple estimate of \bar{w} (Eqs. 8 and 9) does not capture the essential details of the evolution of $\partial\eta_2/\partial t$ during adjustment and the initial convergence or divergence in layer-one $w(0)$ is an overestimate for the interface's average vertical velocity during adjustment. For most tests, however, the ratio of modeled t_{BT} to that predicted from Equation 11 is close to one and the scaling is consistent with the numerical model output.

Next we consider the implications of the dependence of t_{BT} on f , $\Delta\rho$ and R implied by Equation 11 and compare these with the numerical model output. First, Equation 11

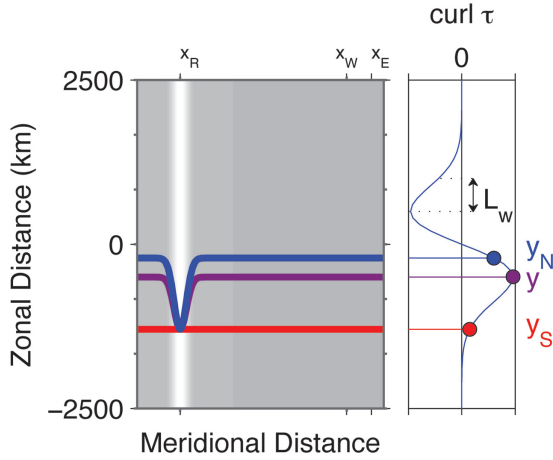


Figure 13. Left: Geostrophic contours connecting the western boundary with the wind patch through a common latitude at the ridge crest: f/h (purple), f/h_1 (red), and f/h_2 (blue). Right: shows the normalized wind stress curl with the curls at y_N , y , and y_S (see text) highlighted. The length scale associated with wind stress curl variations, L_W , is also indicated.

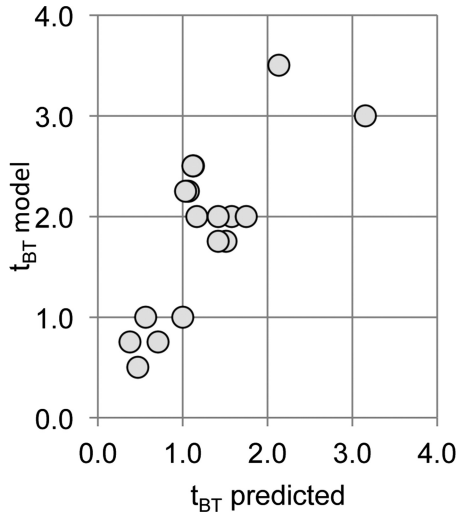


Figure 14. Time for flow to adjust, t_{BT} , predicted by scaling in Equation 11 relative to that output by the model (y). See Table 2 for the complete list of parameters tested.

predicts longer t_{BT} at high latitudes because f increases poleward. This is consistent with model results in Figures 4, 6 and 12, which show slower adjustment towards the north. Second, according to Equation 11, t_{BT} is lower for cases with a greater density contrast between layers (larger g'). The dependence of Equation 11 on $\Delta\rho$ is consistent with the

Table 2. Test of t_{BT} scaling.

| test | y (km) | L_W (km) | W_R (km) | H_1 (m) | $\Delta\rho$ (kg/m^3) | R (m) | u^* | t_{BT} model (yr) | t_{BT} pred. ¹ |
|------|-----------|---------------|---------------|--------------|--|------------|-------|------------------------|--------------------------------|
| 1 | -800 | 2000 | 500 | 800 | 1 | 600 | 2.64 | 2.3 | 1.1 |
| 2 | -1000 | 2000 | 500 | 800 | 1 | 600 | 4.19 | 2.0 | 1.6 |
| 3 | -800 | 1500 | 500 | 800 | 1 | 600 | 3.85 | 2.0 | 1.2 |
| 4 | -1000 | 1500 | 500 | 800 | 1 | 600 | 5.34 | 1.8 | 1.5 |
| 5 | -800 | 1000 | 500 | 800 | 1 | 600 | 5.57 | 2.5 | 1.1 |
| 6 | -1000 | 1000 | 500 | 800 | 1 | 600 | 7.51 | 1.8 | 1.4 |
| 7 | -800 | 500 | 500 | 800 | 1 | 600 | 11.07 | 2.5 | 1.1 |
| 8 | -1000 | 2000 | 500 | 1600 | 1 | 600 | 5.31 | 1.0 | 1.0 |
| 9 | -800 | 1000 | 500 | 800 | 1 | 900 | 5.12 | 2.3 | 1.0 |
| 10 | -1000 | 2000 | 1000 | 800 | 1 | 600 | 4.19 | 3.0 | 3.2 |
| 11 | -800 | 1000 | 500 | 800 | 2 | 600 | 5.57 | 1.0 | 0.6 |
| 12 | -800 | 1000 | 500 | 800 | 3 | 600 | 5.57 | 0.8 | 0.4 |
| 13 | -800 | 2000 | 1000 | 800 | 1 | 600 | 2.64 | 3.5 | 2.1 |
| 14 | -1000 | 1000 | 500 | 800 | 1 | 900 | 7.51 | 2.0 | 1.4 |
| 15 | -1000 | 1000 | 500 | 800 | 2 | 600 | 7.51 | 0.8 | 0.7 |
| 16 | -1000 | 1000 | 500 | 800 | 3 | 600 | 7.51 | 0.5 | 0.5 |
| 17 | -800 | 1000 | 500 | 800 | 1 | 300 | 8.64 | 2.0 | 1.7 |

¹Values are from Eq. 9, normalized by results from test 8.

model results. For $\Delta\rho = 1 \text{ kg m}^{-3}$, the interface displacement at $y = -400 \text{ km}$ takes about 700 days to develop to $\eta_2 = -90 \text{ m}$ (Figure 15a, solid curve). Running the model with $\Delta\rho = 2 \text{ kg m}^{-3}$ and 3 kg m^{-3} (Fig. 15a dashed and dotted curves, respectively) leads to shorter t_{BT} (400 and 250 days, respectively). Furthermore, the associated displacements ($\eta_2 = -40 \text{ m}$ and -30 m) are smaller magnitude than for the case with $\Delta\rho = 1 \text{ kg m}^{-3}$. This is because the same pressure gradient is achieved with smaller magnitude interface displacements, $\Delta\eta_2$, when $\Delta\rho$ is greater.

In contrast to its dependence on f and $\Delta\rho$, model results show t_{BT} is only weakly dependent on ridge height. While R doesn't appear in Equation 11 explicitly, u^* is weakly dependent on R , in part because the deflections of f/h and f/h_2 contours at the ridge – and hence y , y_S and y_N – do depend on R . (In Appendix A.3, Eqs. A-9 and A-10 demonstrate a direct dependence of u^* on R due to constriction of the flow's cross-sectional area at the ridge and an indirect dependence due to deflection of geostrophic contours.) This rather weak dependence of t_{BT} on R predicted by the scaling and born out by the model results is somewhat counterintuitive since for a larger R there clearly must be a larger $\Delta\eta_2$ (and larger pressure gradient) to support the velocity change in the more constricted lower layer. This is demonstrated by running the model with $R = 300 \text{ m}$ and 900 m in addition to the standard run with $R = 600 \text{ m}$ (Figure 15b). Clearly, $\Delta\eta_2$ increases with R (and the latitude of maximum $|\eta_2|$ is farther south for greater R because f/h_2 contours are deflected farther south). However, in all three cases, $|\eta_2|$ is fully developed by day-700 suggesting t_{BT} is

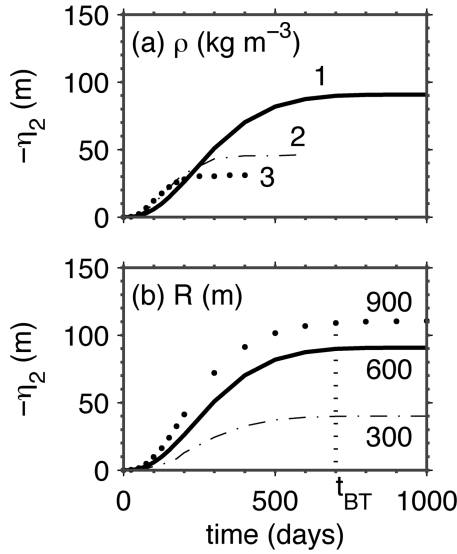


Figure 15. Evolution of $-\eta_2$ for the stationary ridge anomaly that forms on the ridge crest at $y = -400$ km. Results in panel (a) are for $R = 600$ m and three different $\Delta\rho$ values (1 kg m^{-3} , 2 kg m^{-3} , and 3 kg m^{-3}). Results in panel (b) are for $\Delta\rho = 1 \text{ kg m}^{-3}$ and three different R values (600 m, 300 m, and 900 m) with t_{BT} (which is independent of R) indicated. In both cases $x_R = 2,500$, $x_W = 6,000$ km, $x_E = 8,000$ km and $X = 10,000$ km.

indeed largely independent of R . To establish why this increase in $\Delta\eta_2$ with increasing R is *not* accompanied by an increase in t_{BT} as superficially suggested by Equation 8, one must also consider the vertical velocity of the interface. Figure 15b shows the slope, $\partial\eta_2/\partial t$ (*i.e.*, the interface velocity w), does depend on R : larger R leads to greater $|\partial\eta_2/\partial t|$ due to stronger convergence or divergence over the ridge flank. Since the increase in $|w|$ is compensated by a commensurate increase in $\Delta\eta_2$, the ratio in Equation 8 remains essentially unchanged with t_{BT} relatively insensitive to R .

c. Amplitude of T'_{WBC}

During adjustment (*i.e.*, when $0 < t < t_{BT}$) as the initial flow evolves towards the first equilibrium, a barotropic signal develops at the ridge and propagates west along f/h contours (Fig. 10a) resulting in anomalous WBC transport (Fig. 9a). This anomalous transport grows during adjustment and then remains steady from $t = t_{BT}$ until lower-layer flow at the ridge is finally shut down by arrival of the wind-driven baroclinic signal after which the anomalous transport ceases (when $t = t_{EQ}$ as given by Eq. 6, beyond the time frame plotted in Fig. 9). In the previous section we developed a scaling for t_{BT} (Eq. 11). Here we develop a scaling for the magnitude of this anomalous transport, T'_{WBC} , relative to the transport expected for a flat ocean, T_{Sv} where $T'_{WBC} = T_{WBC} - T_{Sv}$ (the final result is given

in Eq. 19). Below we show that the critical parameter for setting T'_{WBC} is not the wind stress curl, but the meridional variation in the wind stress curl.

Two points about adjustment at the ridge provide guidance for the derivation of a scale for T'_{WBC} . First, as flow adjusts and the interface over the ridge gets deformed, η_1 at the crest evolves from its initial barotropic state where $\eta_1 = \eta_{1BT}$ to a state where both barotropic and baroclinic components contribute to total sea surface height at the crest ($\eta_1 = \eta_{1BC} + \eta_{1BT}$). Second, while the initial net flow at the crest (at latitude = y_S) is a response to the wind stress curl at only one latitude (y) connected to the wind-patch by an f/h contour, the adjusted net flow at the crest is a response to wind stress curl at different latitudes (y_S and y_N) connected to the wind patch by f/h_1 and f/h_2 contours in the upper and lower layers, respectively (Fig. 13). Thus, we anticipate that T'_{WBC} will be sensitive to the meridional differences in the wind-stress curl. In the following scale derivation, since it is the barotropic mode that carries transport, we first relate T'_{WBC} to the anomalous, barotropic component of η_1 (*i.e.*, η'_{1BT}) on the offshore edge of the WBC (Eq. 12). Then we relate this η'_{1BT} , which is generated at the ridge, to horizontal velocities at the ridge (Eqs. 13–14). Finally, we connect these velocities at the ridge to the wind forcing over the eastern ocean (Eqs. 15–17) to derive the scaling that relates T'_{WBC} on the western boundary to the wind forcing over the eastern ocean (Eqs. 18 and 19).

We start with the x -momentum equation in each layer and integrate vertically from the surface to $z = -H$ and zonally across the width of the WBC, Δx_{BL} , to obtain an expression for WBC meridional transport. Isolating the anomalous piece of the transport (*i.e.*, T'_{WBC} which is associated with η'_{1BT}) and scaling gives:

$$T'_{WBC} = \frac{gH\Delta x_{BL}}{f} \frac{\partial \eta'_{1BT}}{\partial x} \sim \frac{gH}{f} \eta'_{1BT} \quad (12)$$

where H is the depth of the WBC and η'_{1BT} on the R.H.S. of Equation 12 is the value at the eastern edge of the western boundary layer at latitude = y . (This scaling assumes that η'_{1BT} directly on the western boundary ($x = 0$) is small, which is a good approximation with the no-slip boundary condition.)

Since η'_{1BT} on the R.H.S. of Equation 12 arrives at the offshore side of the WBC by propagating from the ridge along an f/h contour, we next evaluate η'_{1BT} at the ridge crest at latitude = y_S by relating it to the zonal velocities (u_i) over the crest. First we use the thermal wind relationship to determine the baroclinic component of sea surface slope ($\partial \eta_{1BC}/\partial y$) of the adjusted flow at the crest and then we use geostrophy, applied to the upper layer, to determine the adjusted flow's total sea surface slope ($\partial \eta_1/\partial y$). Subtracting ($\partial \eta_1/\partial y - \partial \eta_{1BC}/\partial y$) to isolate the barotropic piece of the sea surface slope gives:

$$\frac{\partial \eta_{1BT}}{\partial y} = \frac{f}{2g} (u_1(x_R, y_S, t_{BT}) + u_2(x_R, y_S, t_{BT})). \quad (13)$$

Equation 12 emphasizes that it is always the barotropic mode that carries the net transport with this mode characterized by that part of the sea surface slope that is not compensated

by the interface slope. The anomalous part of Equation 12, (*i.e.*, that associated with T'_{WBC}) is given by:

$$\frac{\partial \eta'_{1BT}}{\partial y} = \frac{f}{g} \left(\frac{u_1(x_R, y_S, t_{BT}) + u_2(x_R, y_S, t_{BT})}{2} - u_1(x_R, y_S, t = 0) \right), \quad (14)$$

where $u_1(x_R, y_S, 0)$ is the initial, barotropic flow in the upper layer at the ridge crest.

With η'_{1BT} at the crest cast as a function of the zonal flow at the crest in Equation 14, we next relate the layer velocities in Equation 14 to the wind forcing by considering the geostrophic contours that connect the ridge to the wind patch (Fig. 13) and then calculating the interior zonal Sverdrup flow in the flat region between the forcing and the ridge along these contours (*e.g.*, Vallis, 2006, p. 590). The *adjusted* upper-layer flow at the crest in Equation 14 depends on the wind stress curl (applied upstream where $x_W < x < x_E$) at y_S :

$$u_1(x_R, y_S, t_{BT}) = -\frac{\partial}{\partial y} \int_{x_W}^{x_E} \frac{\vec{k} \cdot \nabla \times \vec{\tau}(y_S)}{\rho_o \beta H} dx. \quad (15)$$

The initial barotropic flow in the upper layer at the ridge crest in Equation 14 has a more complicated form than that in Equation 15 since it depends not only on the wind stress curl at y , but also on the constriction of the total flow's cross-sectional area due to the ridge. (An expression for the latter is derived in Appendix A.2 resulting in Eq. A-7.) The initial barotropic flow in the upper layer at the ridge crest is:

$$u_1(x_R, y_S, 0) = -\left(\frac{H}{H-R} \right)^2 \frac{\partial}{\partial y} \int_{x_W}^{x_E} \frac{\vec{k} \cdot \nabla \times \vec{\tau}(y)}{\rho_o \beta H} dx. \quad (16)$$

Likewise, the adjusted lower-layer flow at the crest in Equation 14 depends not only on the wind stress curl at y_N , but also on the constriction of the lower-layer's cross-sectional area. The adjusted lower-layer flow at the crest is:

$$u_2(x_R, y_S, t_{BT}) = -\left(\frac{H_2}{H_2-R} \right)^2 \frac{\partial}{\partial y} \int_{x_W}^{x_B} \frac{\vec{k} \cdot \nabla \times \vec{\tau}(y_N)}{\rho_o \beta H} dx. \quad (17)$$

Combining Equations 15, 16 and 17 with Equation 14 and scaling produces an expression for η'_{1BT} which we then plug into the R.H.S. of Equation 12 to arrive, finally, at the scale for T'_{WBC} :

$$T'_{WBC} \sim \frac{W_W}{\rho_o \beta} \left(\frac{-\vec{k} \cdot \nabla \times \tau(y_S) - \left(\frac{H_2}{H_2-R} \right)^2 \vec{k} \cdot \nabla \times \tau(y_N)}{2} + \left(\frac{H}{H-R} \right)^2 \vec{k} \cdot \nabla \times \tau(y) \right). \quad (18)$$

Here W_w is the zonal width of the wind patch (see Eq. 1). For modest ridges, where $(H_2/(H_2 - R))^2$ and $(H/(H - R))^2$ approach 1, Eq. 18 can be simplified:

$$T'_{WBC} \sim \frac{W_w}{\rho_o \beta} \left(\frac{-\vec{k} \cdot \nabla \times \tau(y_S) - \vec{k} \cdot \nabla \times \tau(y_N)}{2} + \vec{k} \cdot \nabla \times \tau(y) \right). \quad (19)$$

In Equation 19, y , y_S and y_N reflect the flow deflection that occurs at the ridge. (An expression for this deflection, which depends on R and latitude, is given in the Appendix A.2 as Eq. A-4).

According to Equation 19, T'_{WBC} is independent of $\Delta\rho$ between layers. (This is in contrast to t_{BT} , which decreases with increasing $\Delta\rho$, Eq. 11). However, T'_{WBC} does depend on R and on the wind stress curl field. We briefly explore this dependence below and then test the scaling in Equation 19 with several numerical model runs by varying the wind field (L_w), R and $\Delta\rho$.

For modest ridges, if wind stress curl is uniform with latitude, Equation 19 reduces to zero. In this limit, there is no anomalous transport at the western boundary. However, there will be a WBC transport anomaly, even for modest ridges, if the wind stress curl varies over scales that are small relative to the deflection that occurs over the ridge ($\Delta y = y_S - y$). At $y = 0$ (the central latitude of the basin, where $f = f_o$) this deflection scales as:

$$\Delta y \sim \frac{f_o R}{\beta H}. \quad (20)$$

Towards the poles, Δy approaches infinity (because β approaches zero), so essentially any meridional variation in wind stress curl will lead to anomalous WBC transport at high latitudes, even for quite small ridges.

We test the scaling in Equation 19 by comparing the scaling predictions with the numerical model output. Equation 19 is consistent with the model results for a range of parameters (Fig. 16, Table 3). These tests demonstrate the effects on T'_{WBC} of 1) the wind field (by varying the length scale of the wind stress, L_w , see Eq. 3); 2) the deflection (by varying R); and 3) $\Delta\rho$. Considering first the effect of the wind field with $R = 300$ m, the modeled T'_{WBC} at $y = -500$ km (yellow filled symbols in Fig. 16) decreases as L_w increases (1,000, 1,500 to 2,000 km). This is because the meridional variation in wind stress curl decreases as L_w increases, and is consistent with the scaling prediction from Equation 19. Considering next the effect of R , for $L_w = 1,500$ km as R increases (300, 600 to 900 m; yellow, orange and red filled squares, respectively, in Fig. 16) both the modeled T'_{WBC} and that predicted from Equation 19 increase at $y = -500$ km, reflecting the increased deflection of geostrophic contours as R increases. Furthermore, this dependence on R is also apparent in Figure 17, which shows the time-evolution of T_{WBC} for different R . (In addition, this plot reiterates that t_{BT} is largely independent of R , consistent with Eq. 11.) Finally, modeled T'_{WBC} is independent of density difference, consistent with Equation 19 in which $\Delta\rho$ does not appear. This is confirmed by the evolution of T_{WBC} plotted in Figure 18: though t_{BT} varies with $\Delta\rho$,

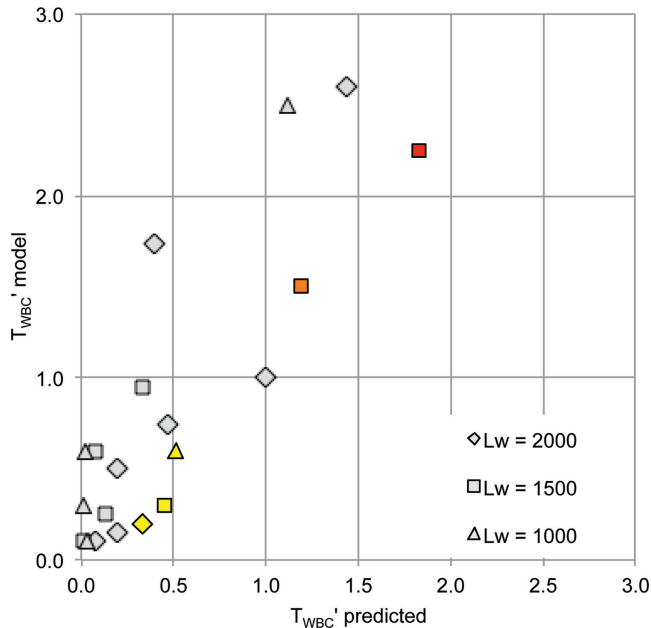


Figure 16. Transport anomaly, T'_{WBC} , predicted by scaling in Equation 19 relative to that output by the model (Sv). Some experiments are highlighted (see text): yellow filled symbols are $R = 300$ m, orange is $R = 600$ m and red is $R = 900$ m. See Table 3 for the complete list of parameters tested.

T'_{WBC} does not (these experiments would fall on top of one another if they were included in Fig. 16).

In some numerical experiments, the deflection is large relative to the meridional extent of the Gaussian wind patch. In these cases, the scaling in Equation 19 under-predicts the modeled T'_{WBC} (e.g., points falling above a 1:1 line in Fig. 16). This is most likely because the deflection at the ridge is so large (relative to the wind patch) that the f/h_1 contour that passes through y_s is outside of the wind patch at $x_W < x < x_E$. In these cases, L_w is not the appropriate length scale for ∂y in Equation 15 and the scaling for T'_{WBC} in Equations 18 and 19 should take a more complicated form.

5. Summary

Despite significant simplifications (linear equations, idealized forcing and topography), the two-layer model used here is useful for exploring phenomena that may have analogs in the real ocean. With the modest ridge heights modeled here, interaction of wind-forced barotropic planetary Rossby waves with topography does not lead to blocking of the barotropic response (though we note, with taller ridges: 1) f/h contours may stretch into an equatorial waveguide, thereby blocking the westward propagation of the barotropic

Table 3. Test of T'_{WBC} scaling.

| test ¹ | R (m) | L _W (km) | y (km) | Δ _y (km) | T' _{sv} model (Sv) | T' _{sv} predicted ² |
|-------------------|-------|---------------------|--------|---------------------|-----------------------------|---|
| 1 | 300 | 2000 | -1000 | -201 | 0.1 | 0.1 |
| 2 | 600 | 2000 | -1000 | -402 | 0.5 | 0.2 |
| 4 | 300 | 2000 | -800 | -216 | 0.2 | 0.2 |
| 5 | 600 | 2000 | -800 | -432 | 0.7 | 0.5 |
| 6 | 900 | 2000 | -800 | -649 | 1.7 | 0.4 |
| 7 | 300 | 2000 | -500 | -239 | 0.2 | 0.3 |
| 8 | 600 | 2000 | -500 | -477 | 1.0 | 1.0 |
| 9 | 900 | 2000 | -500 | -716 | 2.6 | 1.4 |
| 10 | 300 | 1500 | -1000 | -201 | 0.1 | 0.0 |
| 11 | 600 | 1500 | -1000 | -402 | 0.6 | 0.1 |
| 13 | 300 | 1500 | -800 | -216 | 0.3 | 0.1 |
| 14 | 600 | 1500 | -800 | -432 | 1.0 | 0.3 |
| 16 | 300 | 1500 | -500 | -239 | 0.3 | 0.5 |
| 17 | 600 | 1500 | -500 | -477 | 1.5 | 1.2 |
| 18 | 900 | 1500 | -500 | -716 | 2.3 | 1.8 |
| 19 | 300 | 1000 | -1000 | -201 | 0.1 | 0.0 |
| 20 | 600 | 1000 | -1000 | -402 | 0.6 | 0.0 |
| 22 | 300 | 1000 | -800 | -216 | 0.3 | 0.0 |
| 25 | 300 | 1000 | -500 | -239 | 0.6 | 0.5 |
| 26 | 600 | 1000 | -500 | -477 | 2.5 | 1.1 |

¹All tests were with $\Delta\rho = 1 \text{ kg m}^{-3}$, $W_R = 500 \text{ km}$, $H_1 = 800 \text{ m}$, $H_2 = 3200 \text{ m}$.

²Values are from Eq. 19, normalized by results from test 8.

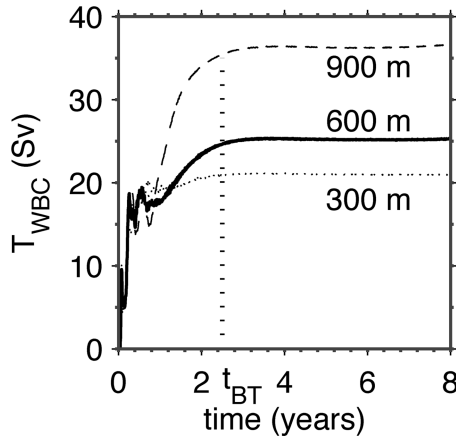


Figure 17. Evolution of T_{WBC} at $y = -500 \text{ km}$ for the three different R values (300 m, 600 m and 900 m). For each run: $\Delta\rho = 1 \text{ kg m}^{-3}$, $x_R = 3,600 \text{ km}$, $x_W = 17,000 \text{ km}$, $x_E = 19,000 \text{ km}$ and $X = 20,000 \text{ km}$. Eventually, beyond the time plotted here, T_{WBC} for all three cases equals T_{sv} predicted by Equation 1 when the lower layer is shut-down by arrival of the wind driven baroclinic Rossby waves and flow no longer interacts with the topography.

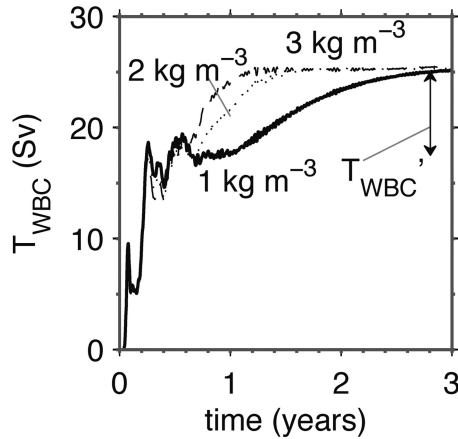


Figure 18. Evolution of T_{WBC} at $y = -500$ km for the three different $\Delta\rho$ values as indicated on the plot. The magnitude of the anomalous T'_{WBC} (which is independent of $\Delta\rho$) is also indicated. For each run: $R = 600$ m, $x_R = 3,600$ km, $x_W = 17,000$ km, $x_E = 19,000$ km and $X = 20,000$ km.

response and 2) the linear assumptions in the model will break down). Rather than being blocked by modest ridges, barotropic Rossby waves establish T_{WBC} rapidly in the model. Further, this interaction causes stationary and propagating ridge-generated anomalies as the flow adjusts. Based on these model results, one expects evidence in ocean observations of 1) a rapid WBC response to remote wind forcing and 2) baroclinic variability generated along mid-ocean ridges. Indeed such rapid (barotropic) responses to wind forcing are reported based on observations from the Pacific marginal seas (Gordon and Giulivi, 2004; Han and Huang, 2008; Andres et al., 2011). The model result that the barotropic mode interacts with mid-basin topography to generate at least some of the ocean's ubiquitous slow, westward propagating features as propagating ridge-generated anomalies may account for satellite altimetry observations in which baroclinic anomalies can be traced back to a ridge or seamount chain (Fig. 1 and Chelton and Schlax, 1996). Despite their effect on WBCs, the ocean's barotropic responses (whether wind-driven or ridge-generated) are difficult to observe in the ocean interior because 1) $\eta_{1BT} \ll \eta_{1BC}$ and 2) barotropic wave fronts propagate very rapidly.

According to the model, T_{WBC} transport in a flat ocean obeys the Sverdrup balance and is given by Equation 1. For an ocean with mid-basin topography, however, this Sverdrup balance is disrupted due to the arrival of propagating ridge-generated anomalies. These ridge-generated anomalies affect both the vertical structure of the WBC (via baroclinic anomalies), and also the net transport there (via barotropic anomalies), such that, for a time (until the wind-driven baroclinic Rossby waves reach the ridge), the balance in Equation 1 does not hold. In the ocean, arrival of propagating ridge-generated anomalies along the western boundary might explain anomalous lags observed between wind-forcing and WBC

responses which are too long to be due to barotropic waves and too short to be due to wind-forced baroclinic Rossby waves (Hill et al., 2008). This suggests that at intermediate delays relative to shifts in the wind forcing (at interannual scales) it is important to consider the coupling between barotropic and baroclinic modes in the presence of topography.

Finally, we note that the model used here is linear so the adjusted flow in either layer is along f/h_i contours. In a high-resolution and nonlinear model, eddies likely play an important role. Convergence of eddy potential vorticity flux is effective in forcing transport over a topographic barrier, as demonstrated in a two-layer model by Kida et al. (2009). In addition, while the model here is forced with a steady wind, periodic wind-forcing may result in the blocking of some frequencies at the ridge. Periodic forcing has been examined, for example, by Veronis and Stommel (1956) for a flat ocean and by Wang and Koblinsky (1994) for an ocean with a top hat shaped ridge. The higher order, non-linear dynamics and the effects of periodic forcing will be considered further in future studies.

Acknowledgments. We thank the *JMR* Editor, Ken Brink, and two anonymous reviewers for constructive comments on this manuscript. We also appreciate suggestions from Mike Spall on a previous version of the manuscript. Support for this work was provided by the National Science Foundation through grant OCE-1028739 and the WHOI Ocean and Climate Change Institute.

APPENDIX

A.1 Model formulation

The model used here is a linear primitive equations model on a beta plane with two active layers and topography that extends only into the lower layer. U_i and V_i are depth-integrated zonal and meridional velocities, respectively, for each layer. In the linear formulation $U_i = u_i \cdot h_i(0)$ and $V_i = v_i \cdot h_i(0)$ where u_i and v_i are zonal and meridional velocities, respectively, in each layer.

The depth-integrated x and y components of the linear momentum equations in each layer are:

$$\frac{\partial U_i}{\partial t} - (f_o + \beta y)V_i = -\frac{h_i(0)}{\rho_o} \frac{\partial p_i}{\partial x} + A \nabla^2 U_i - B \nabla^4 U_i + \frac{\tau_i^x}{\rho_o} \quad (\text{A-1})$$

$$\frac{\partial V_i}{\partial t} + (f_o + \beta y)U_i = -\frac{h_i(0)}{\rho_o} \frac{\partial p_i}{\partial y} + A \nabla^2 V_i - B \nabla^4 V_i + \frac{\tau_i^y}{\rho_o} \quad (\text{A-2})$$

The Coriolis parameter at a reference latitude, θ_0 , is $f_0 = 2\Omega \sin \theta_0$ where Ω is the earth's rotation rate ($7.2722 \times 10^{-5} \text{ s}^{-1}$). The variation of Coriolis parameter about that latitude is β , where $\beta = 2\Omega \cos \theta_0/a$ and a is the earth's radius (6,378 km). The reference density, ρ_0 , is $1,028 \text{ kg m}^{-3}$. Pressure in each layer is p_i . The zonal and meridional components of stress in each layer are τ_i^x and τ_i^y . A and B are the constant coefficients for the Laplacian and biharmonic viscosity terms, respectively. The pressure terms in Equations (A-1) and (A-2) are obtained by solving the hydrostatic balance in each layer.

Wind stress is applied at the surface and since the lower layer does not outcrop, $\tau_2^x = \tau_2^y = 0$. No-slip and no-normal-flow boundary conditions are applied on the vertical boundaries of the model domain, but bottom friction is not included.

The depth-integrated continuity equation for each layer is:

$$\frac{\partial h'_i}{\partial t} = - \left(\frac{\partial U_i}{\partial x} + \frac{\partial V_i}{\partial y} \right). \quad (\text{A-3})$$

Calculations are performed on a C-grid (Arakawa and Lamb, 1977). The model time-step, dt , is 15 seconds. Such a small time step is required for stability, satisfying the CFL condition (Courant et al., 1928).

Horizontal viscosity, A , is $2,000 \text{ m}^2\text{s}^{-1}$ and the biharmonic viscosity coefficient, B , is $10^{12} \text{ m}^4 \text{ s}^{-1}$ (though for the coarse model resolution used here, results are insensitive to this parameter). Use of large A is common in coarse resolution models to help resolve the width of the frictional Munk boundary layer along the basin's western boundary. The model does not include vertical viscosity.

A.2 Deflection over the ridge on a beta-plane

Contours of constant f/h and f/h_2 are curved southward over a ridge to a maximum deflection, Δy , at the crest (Fig. A1). On a beta-plane, Δy increases linearly with latitude:

$$\Delta y = -\frac{R}{H} \left(y + \frac{f_o}{\beta} \right). \quad (\text{A-4})$$

Therefore, f/h contours (or f/h_2 contours) are more closely packed over the ridge than over the flat ocean. The ratio of spacing between neighboring f/h contours in the flat region, L_F , to their spacing at the crest, L_R , is

$$\frac{L_F}{L_R} = \frac{H}{H - R}. \quad (\text{A-5})$$

This is independent of latitude on a beta plane. In the analogous relationship for f/h_2 contours, H in Equation A-5 is replaced with H_2 .

When barotropic flow contained between neighboring f/h contours encounters the ridge, the area perpendicular to the horizontal flow is decreased not only in the vertical dimension (because of the ridge), but also in the horizontal (because $L_R < L_F$). The ratio of the area in the flat region A_F to that at the ridge crest A_R (assuming $\eta_1 \ll H$) is:

$$\frac{A_F}{A_R} = \left(\frac{H}{H - R} \right)^2 \quad (\text{A-6})$$

Hence, for non-divergent horizontal flow, the ratio of zonal velocity, u , in the flat region (x_F, y) to that at the crest ($x_R, y + \Delta y$) must be:

$$\frac{u(x_F, y)}{u(x_R, y + \Delta y)} = \left(1 - \frac{R}{H} \right)^2. \quad (\text{A-7})$$

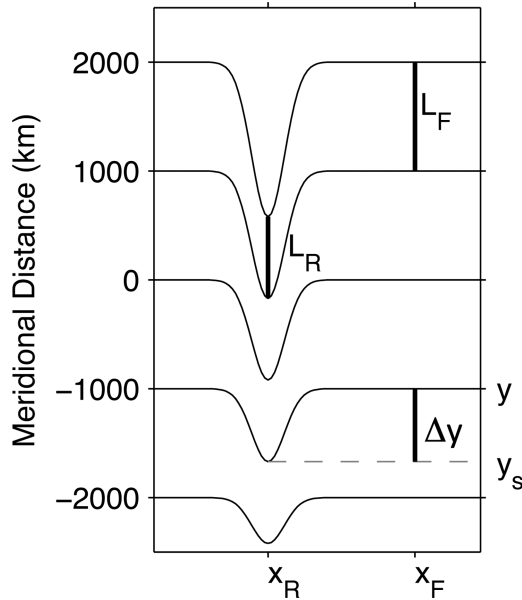


Figure A1. Deflection of f/h contours over a ridge centered at x_R . $\Delta y = y_s - y$, L_R is the spacing of f/h contours at the crest where $x = x_R$, and L_F is the spacing of f/h contours in the flat region where $x = x_F$.

Analogous equations can be written for lower-layer flow, u_2 , contained between neighboring f/h_2 contours (assuming $\eta_2 \ll H_2 - \eta_b$) with H replaced by H_2 in A-6 and A-7.

A.3 Recasting u^* as a function of velocities in the flat region

The ratio of the vertical shear of the adjusted ($t = t_{BT}$) zonal flow at the ridge crest to the initial ($t = 0$) horizontal divergence or convergence in layer-one on the ridge’s flank is:

$$u^* = \frac{u_2(x_R, y_S, t_{BT}) - u_1(x_R, y_S, t_{BT})}{u_1(x_R, y_S, t = 0) - u_1(x_F, y, t = 0)} \tag{A-8}$$

Rearranging the denominator of A-8 and combining with A-7 gives:

$$u_1(x_R, y_S, t = 0) - u_1(x_F, y, t = 0) = u_1(x_F, y, t = 0) \left(\left(\frac{H}{H - R} \right)^2 - 1 \right) \tag{A-9}$$

Then considering the numerator of Equation A-9, we note that: 1) $u_1(x_R, y_S, t_{BT}) = u_1(x_F, y_S, t_{BT})$ because there is no divergence in the upper layer once equilibrium is reached at t_{BT} and 2) $u_1(x_F, y, t_{BT}) = u_2(x_F, y, t_{BT})$ because the flow between the topography and the wind patch is barotropic (until the wind-driven baroclinic signal arrives). Using this with

Equation A-7 cast for the lower layer and combining the result with Equations A-8 and A-9 gives:

$$u^* = \frac{u_1(x_F, y_N) \left(\frac{H_2}{H_2 - R} \right)^2 - u_1(x_F, y_S)}{u_1(x_F, y) \left[\left(\frac{H}{H - R} \right)^2 - 1 \right]} \quad (\text{A-10})$$

In Equation A-10, we treat the velocities at x_F as independent of time since we restrict our analysis to the region east of the topography where the wind-driven baroclinic Rossby waves have not yet arrived.

REFERENCES

- Anderson, D. T. L. and A. E. Gill. 1975. Spin-up of a stratified ocean, with applications to upwelling. *Deep Sea Res.*, 22, 583–596.
- Andres, M.; Y.-O. Kwon and J. Yang. 2011. Observations of the Kuroshio's barotropic and baroclinic responses to basin-wide wind forcing. *J. Geophys. Res.*, 116, C04011, doi:10.1029/2010JC006863.
- Arakawa, A. and V. R. Lamb. 1977. Computational design of the basic dynamical processes of the UCLA General Circulation Model. *Methods Comput. Phys.*, 17, 174–265.
- Barnier, B. 1988. A numerical study on the influence of the Mid-Atlantic Ridge on nonlinear first-mode baroclinic Rossby waves generated by seasonal winds. *J. Phys. Oceanogr.*, 18, 417–433.
- Brink, K. H. 1989. Evidence for wind-driven current fluctuations in the western North Atlantic. *J. Geophys. Res.*, 94, 2029–2044.
- Chelton, D. B. and M. G. Schlax. 1996. Global observations of oceanic Rossby waves. *Science*, 272, 234–237.
- Courant, R.; K. O. Friedrichs and H. Lewy. 1928. Über die partiellen Differenzgleichungen der mathematische Physik. *Math. Ann.*, 100, 32–74.
- Deser, C.; M. A. Alexander and M. S. Timlin. 1999. Evidence for a wind-driven intensification of the Kuroshio Current Extension from the 1970s to the 1980s. *J. Climate*, 12, 1697–1706.
- Gill A. 1982. *Atmosphere-Ocean Dynamics*. Academic Press, 662 pp.
- Gordon, A. L. and C. F. Giulivi. 2004. Pacific decadal oscillation and sea level in the Japan/East Sea. *Deep Sea Res. I*, 51, 653–663.
- Han, G. and W. Huang. 2008. Pacific decadal oscillation and sea level variability in the Bohai, Yellow and East China Seas. *J. Phys. Oceanogr.*, 38, 2772–2783.
- Hill, K. L.; S. R. Rintoul; R. Coleman and K. R. Ridgway. 2008. Wind forced low frequency variability of the East Australia Current. *Geophys. Res. Lett.*, 35, L08602, doi:10.1029/2007GL032912.
- Kida, S.; J. Yang and J. F. Price. 2009. Marginal sea overflows and the upper ocean interaction. *J. Phys. Oceanogr.*, 39, 387–403, doi:10.1175/2008JPO3934.1.
- Owen, G. W.; A. J. Willmott; I. D. Abrahams and H. Mansley. 2005. The scattering of Rossby waves from finite abrupt topography. *Geophys. Astrophys. Fluid Dyn.*, 99(3), doi: 10.1080/03091920500087690.
- Owen, G. W.; I. D. Abrahams; A. J. Willmott and C. W. Hughes. 2002. On the scattering of baroclinic Rossby waves by a ridge in a continuously stratified ocean. *J. Fluid Mech.*, 465, doi:10.1017/S0022112002001027.
- Pedlosky, J. and M. Spall. 1999. Rossby normal modes in basins with barriers. *J Phys. Oceanogr.*, 29, 2332–2349.
- Price, J. M. and L. Magaard. 1986. Interannual baroclinic Rossby waves in the Midlatitude North Atlantic. *J. Phys. Oceanogr.*, 16, 2061–2070.

- Qiu, B. 2003. Kuroshio Extension variability and forcing of the Pacific decadal oscillations: responses and potential feedback. *J. Phys. Oceanogr.*, 33, 2465–2482.
- Qiu B. and S. Chen. 2005. Variability of the Kuroshio Extension Jet, recirculation gyre, and mesoscale eddies on decadal time scales. *J. Phys. Oceanogr.*, 35, 2090–2103.
- Smith, W. H. F. and D. T. Sandwell. 1994. Bathymetric prediction from dense satellite altimetry and sparse shipboard bathymetry. *J. Geophys. Res.*, 99, 21803–21824.
- Sturges W. and B. G. Hong. 1995. Wind forcing of the Atlantic thermocline along 32°N at low frequencies. *J. Phys. Oceanogr.*, 25, 1706–1715.
- Tallieux, R. and J. C. McWilliams. 2000. Accretion, creation, and depletion of wind-driven baroclinic Rossby waves over an ocean ridge. *J. Phys. Oceanogr.*, 30, 2186–2213.
- Tanaka, K. and M. Ikeda. 2004. Propagation of Rossby waves over ridges excited by interannual wind forcing in a western North Pacific model. *J. Phys. Res.*, 60, 329–340.
- Vallis, G. 2006. *Atmospheric and Oceanic Fluid Dynamics Fundamentals and Large Scale Circulation*. Cambridge University Press, 745 pp.
- Veronis, G. and H. Stommel. 1956. The action of variable wind stresses on a stratified ocean. *J. Marine Res.*, 15, 43–75.
- Wang, L. and C. J. Koblinsky. 1994. Influence of mid-ocean ridges on Rossby waves. *J. Geophys. Res.*, 99, 25,143–25,153.
- Yang, J. 2003. On the importance of resolving the western boundary layer in wind-driven ocean general circulation models. *Ocean Modelling*, 5, 357–379, doi:10.1016/S1463-5003(02)00058-6.

Received: *Oct. 25, 2012*; revised: *April 2, 2013*.

